Dual-Band Terahertz Auto-Focusing Airy Beam Based on Single-Layer Geometric Metasurfaces with Independent Complex Amplitude Modulation at Each Wavelength

Tailei Wang, Guohua Zhai, Rensheng Xie, Shouzheng Zhu, Jianjun Gao, Sensong An, Bowen Zheng, Hang Li, Yong Liu, Hualiang Zhang,* and Jun Ding**

The Airy beam has attracted considerable interests due to its remarkable non-diffracting, self-bending, and self-healing properties. An auto-focusing Airy (AFA) beam can be achieved by constructing two counter-propagation Airy beams, which is a novel method to generate focusing effect. Traditionally, because of the complexity of the generation mechanism, it is hard to realize the Airy beam with complex amplitude modulation. The reported ones usually require bulky optical systems and typically work at one single wavelength. Here, a general scheme is proposed to launch dual-band Airy and AFA beams based on the single-layer geometric metasurface, consisting of a newly designed meta-atom that can realize independent complex amplitude modulations at two arbitrary terahertz wavelengths. Based on the proposed meta-atom, the aforementioned attractive properties of the Airy beam are demonstrated at two terahertz wavelengths. Besides, the dual-band AFA beams are illustrated to have the practically important adjustability of the focal length. Furthermore, owing to the self-healing property, the proposed focusing scheme (i.e., AFA beam) shows a much better capability of circumventing the PEC obstacles compared to the conventional metalens, which could have potential applications in various important scenarios such as biomedical imaging/therapy and nondestructive evaluation with compact size and multiwavelength functionalities.

The non-dispersion Airy wave packet with curved propagation trajectory was first predicted theoretically by Berry and Balazs,[1] which demonstrated that the Schrodinger equation could possess an Airy function form solution. Although the ideal Airy wave packet is associated with infinite energy, the finite-energy Airy beams were observed experimentally,[2,3] which have attracted a lot of attentions due to their distinct propagation properties (e.g., self-bending without any external potential). In addition, the focusing characteristic of the optical beam has always been of great practical importance. In contrast to the traditional focusing lens, a different scheme of focusing can be achieved by adopting two counter-propagating Airy beams to form an auto-focusing Airy (AFA) beam.[4,5] The AFA beam could be critical in many optical applications, such as optical trapping,[6] and the generation of light bullet.[7] In general, the Airy beam and AFA beam could be generated by various ways including spatial light modulator[8,9] and liquid crystal.[10] However, these methods usually require bulky Fourier transform system and long working distance, which make them bulky and hard to be integrated with other optical systems.

Metasurfaces comprising an array of engineered subwavelength resonators (meta-atoms or unit cells) on an ultra-thin interface have evoked enormous interest for their abilities to modulate the phase, amplitude, polarization, and dispersion of the incident electromagnetic waves,[11–13] which could provide a compact way to launch Airy beams and AFA beams. By properly arranging the judiciously designed meta-atoms, which can be treated as the secondary sources at the interface according to the Huygens' principle, the incident wavefront can be manipulated at will and many traditional functionalities achieved by bulky components can be realized in ultra-thin devices, such as beam manipulations,[14–17] cloaking,[18–20] flat metasurface-based lenses (metalenses),[21–24] and holography[25–28]. Recently, several ultrathin Airy beam generators based on metasurfaces have been presented.[29–33] However, most of the reported Airy beams only operate at a specific and single wavelength due to the dispersive nature of metasurface. Although several achromatic metasurface-based devices have been reported[34–36] very recently, most of them only considered phase modulations. However, the amplitude modulation could be of great significance for

---

T. Wang, Dr. G. Zhai, R. Xie, Dr. S. Zhu, Dr. J. Gao, Dr. J. Ding
Shanghai Key Laboratory of Multidimensional Information Processing
East China Normal University
Shanghai 200241, China
E-mail: jding@ee.ecnu.edu.cn

S. An, B. Zheng, H. Li, Dr. H. Zhang
Department of Electrical and Computer Engineering
The University of Massachusetts Lowell
Lowell, MA 01854, USA
E-mail: hualiang_zhang@uml.edu

Y. Liu
Army Engineering University of PLA
Nanjing, China
E-mail: liuyong4425@sina.com

The ORCID identification number(s) for the author(s) of this article can be found under https://doi.org/10.1002/adts.201900071

DOI: 10.1002/adts.201900071

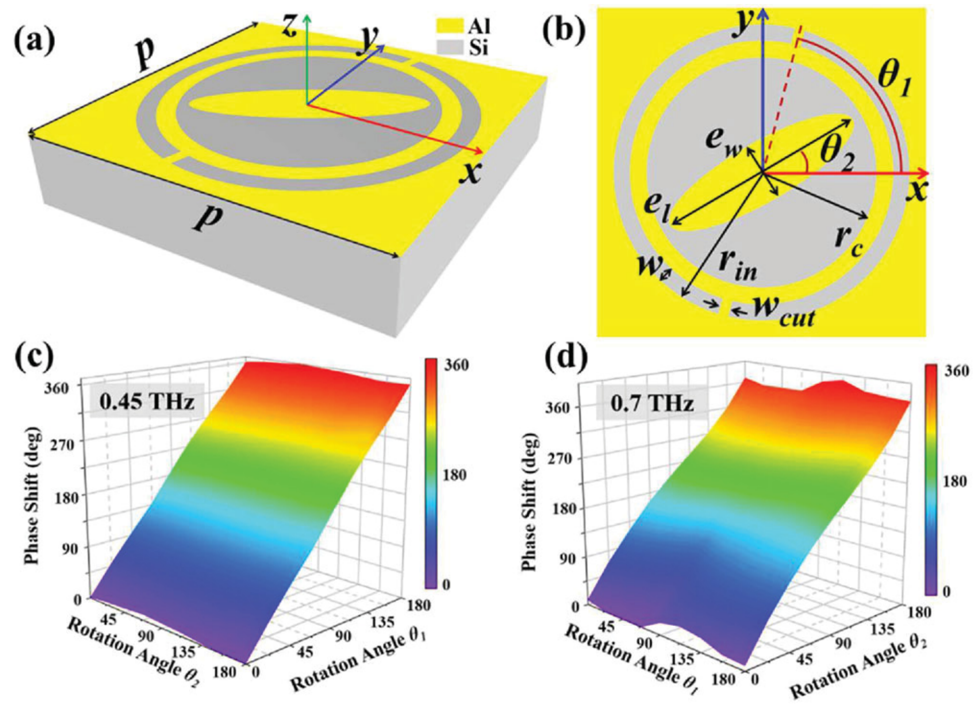

Figure 1. The a) 3D and b) top views of the proposed dual-band unit cell (meta-atom); c) the geometric phase shift by rotating angle θ_1 with a fixed θ_2 at 0.45 THz under a RCP incidence; d) the phase shift by rotating angle θ_2 with a fixed θ_1 at 0.7 THz under a RCP incidence.

better performance or new functionalities. For example, with simultaneous phase and amplitude modulations (i.e., complex amplitude modulation), the higher order diffraction can be realized[37] and the holographic imaging quality could be improved compared to that with the phase only modulation.[38]

Here, we propose a general method for realizing dual-band Airy beams and AFA beams based on geometric metasurfaces with independent complex amplitude modulations at two arbitrary THz wavelengths. The meta-atom (i.e., unit cell) is composed of a modified double-C-slot (MDCS) resonator and an elliptical nanorod resonator located in the middle of a circular hole, which utilizes both electric and magnetic resonances in a deep subwavelength scale. The independent phase and amplitude modulations at two THz frequencies can be achieved by rotating and finely tuning the sizes of the slot/nanorod resonators, respectively. A dual-band Airy beam generator based on the proposed meta-atom is firstly designed to demonstrate the non-diffracting, self-healing, and self-bending features at two THz frequencies. Then, several dual-band AFA beams with different focal positions are realized by varying the bending directions of the Airy beams, which are demonstrated and verified through both theoretical calculations and full-wave simulations. It is found that the AFA beam has a larger depth of focus (DOF) compared to the conventional metalens, which could be of great interest for many practical applications such as medical imaging and nondestructive detections. Moreover, the distinctive self-healing property of the AFA beam is also revealed through several scenarios presented with different sized obstacles. In contrast to the conventional metalens, the dual-band AFA beam shows a much better capability of circumventing the obstacles at both operating THz frequencies.

To design the meta-atoms, the metallic resonators or antennas[37,39] and the Babinet-inverted resonators or slot antennas[40,41] are two general types of resonators that are based on the electric and magnetic resonances, respectively. Usually, it is hard to achieve dual-band functionalities by merely putting together two resonators of the same type in a unit cell because of the strong coupling. Thus, spatial multiplexing[42] or shared aperture[43] are two common ways for multiband operations with the same type of resonators, which would lead to lower efficiency at least at one frequency or larger dimension. The proposed dual-band meta-atom utilizes both electrical and magnetic resonances in a deep subwavelength dimension, which could still make the dual-band functionalities independent. **Figure 1**a,b demonstrates the 3D and top view of the single-layer dual-band meta-atom. It is composed of an elliptic nanorod resonator and a MDCS resonator as illustrated in Figure 1b. The MDCS resonator consists of two symmetric C-shape slots and a circular hole in the middle. The metallic layer made of aluminum with a conductivity of $\sigma = 3.72 \times 10^7$ Sm^{-1} is backed by a silicon substrate with a permittivity of 11.9. The outer radius of the C-slot and the radius of the circular hole are denoted as r_{in} and r_c, respectively. The width of the slot and the gap width between the two slots are denoted as w and w_{cut}, respectively. In Figure 1b, the MDCS resonator is rotated by an angle of θ_1 with respect to x-axis. Besides, Figure 1b also depicts an elliptic nanorod resonator with a rotation angle of θ_2 with respect to the x-axis. The major and minor axes of the ellipse are denoted as e_l and e_w, respectively. In this work, the periodicity of the meta-atom p is fixed as 100 µm and the two arbitrary working frequencies are set as $f_1 = 0.45$ THz ($\lambda_1 = 666.7$ µm) and $f_2 = 0.7$ THz ($\lambda_2 = 428.6$ µm). When a beam of circularly polarized (CP) light is incident onto an resonator,

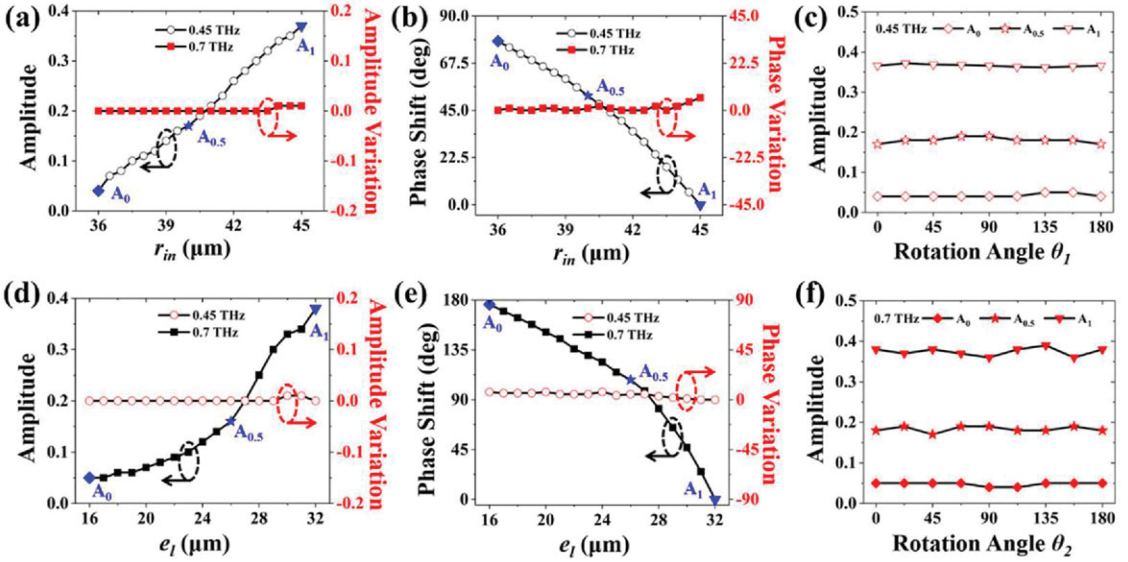

Figure 2. a) Transmission amplitude at 0.45 THz and amplitude variation at 0.7 THz for different outer radius of the slot resonator r_{in}. b) Phase shift at 0.45 THz and phase variation at 0.7 THz for different outer radius of the slot resonator r_{in}. c) Three-level amplitude modulations at 0.45 THz for different rotation angle θ_1. d) Transmission amplitude at 0.7 THz and amplitude variation at 0.45 THz for different nanorod length e_l. e) Phase shift at 0.7 THz and phase variation at 0.45 THz for different nanorod length e_l. f) Three-level amplitude modulations at 0.7 THz for different rotation angle θ_2.

it is partially converted into the opposite helicity of the CP light with an abrupt phase change φ completely determined by the orientation of the resonator,[44] which is called geometric phase or Pancharatnam–Berry phase.[45,46] For such a resonator, the relationship between the imparted geometric phase shift φ and the orientation θ is governed by $\varphi = 2\sigma\theta$, where $\sigma = \pm 1$ corresponds to the helicity state of right-/left-handed circularly polarized (RCP/LCP) incident wave and θ corresponds to the orientation of the resonator.[47–49] Here, positive rotation angle refers to clockwise orientation, and negative refers to counterclockwise. Typically, such phase is geometric in nature and wavelength independent. Moreover, the cross-polarized transmission amplitudes are almost kept constant for different orientations, which is desirable for the metasurface design. Thus, the 2π phase modulations for the lower and higher frequencies of the proposed meta-atom can be achieved by rotating the angles θ_1 and θ_2, respectively.

To get the transmission phase and amplitude of the metasurface, full-wave simulations are carried out by using a commercial software package (CST Microwave Studio), in which the unit cell boundaries are applied to the x- and y-directions, and two Floquet ports are applied to the $+z$ and $-z$ directions. Figure 1c (Figure 1d) plots the geometric phase shift at 0.45 THz (0.7 THz) of the transmitted LCP wave by rotating θ_1 (θ_2) with fixed θ_2 (θ_1) under a RCP incidence. It can be seen from Figure 1c that the whole 2π phase shift can be approximated at 0.45 THz by rotating θ_1 for a fixed θ_2 with a 22.5° phase interval. Besides, the amplitude is kept almost constant due to the geometric phase (not shown here). Similar conclusion can be drawn at 0.7 THz from Figure 1d.

Table 1. Geometric parameters for three-level amplitude modulations at two THz frequencies (unit: μm).

	r_{in}	r_c	w	w_{cut}	e_l	e_w
A_0	34	30	3	3	12	9
$A_{0.5}$	40	30	5	3	26	9
A_1	45	35	5	3	32	9

Furthermore, the amplitude modulation at 0.45 THz and 0.7 THz can be realized by changing the dimensions of the slot resonator and the nanorod. **Figure 2**a,b plots the cross-polarized transmission amplitude and phase shift at 0.45 THz together with amplitude and phase variations at 0.7 THz by changing r_{in}, respectively. Figure 2a illustrates that the transmission amplitude can be tailored from a low level (≈0.04) to a high level (≈0.4) continuously by varying r_{in} without affecting the amplitude response at 0.7 THz, thus, a multilevel amplitude modulation can be readily achieved at 0.45 THz. Figure 2b further demonstrates that the phase response at 0.7 THz would not be affected by changing r_{in}, either. Besides, although the imparted phase shift at 0.45 THz changes as varying r_{in} only, any required phase shift can still be obtained by compensating a preset rotation angle ahead according to the geometric phase principle. Figure 2c plots three-level amplitude modulations (labeled as A_1, $A_{0.5}$, and A_0 in Figure 2a,b) with different orientation angle of θ_1 at 0.45 THz, in which only small fluctuations for different θ_1 can be observed at each level. Similar conclusions can be drawn at 0. 7 THz from Figure 2d,f. By considering Figures 1 and 2 together, one can conclude that complex amplitude modulations can be realized independently at the two operating THz frequencies. Nevertheless, in the design procedure, the radius of the circular hole r_c is of importance to finely tune the coupling between the two resonators.[31,50] The optimized geometrical parameters of the meta-atom that achieves three-level amplitude modulations are listed in **Table 1**. It is worth mentioning that the dual-band cross-polarized conversion efficiencies could reach about 0.4 at both frequencies, which is comparable to the reported single-layer single-wavelength

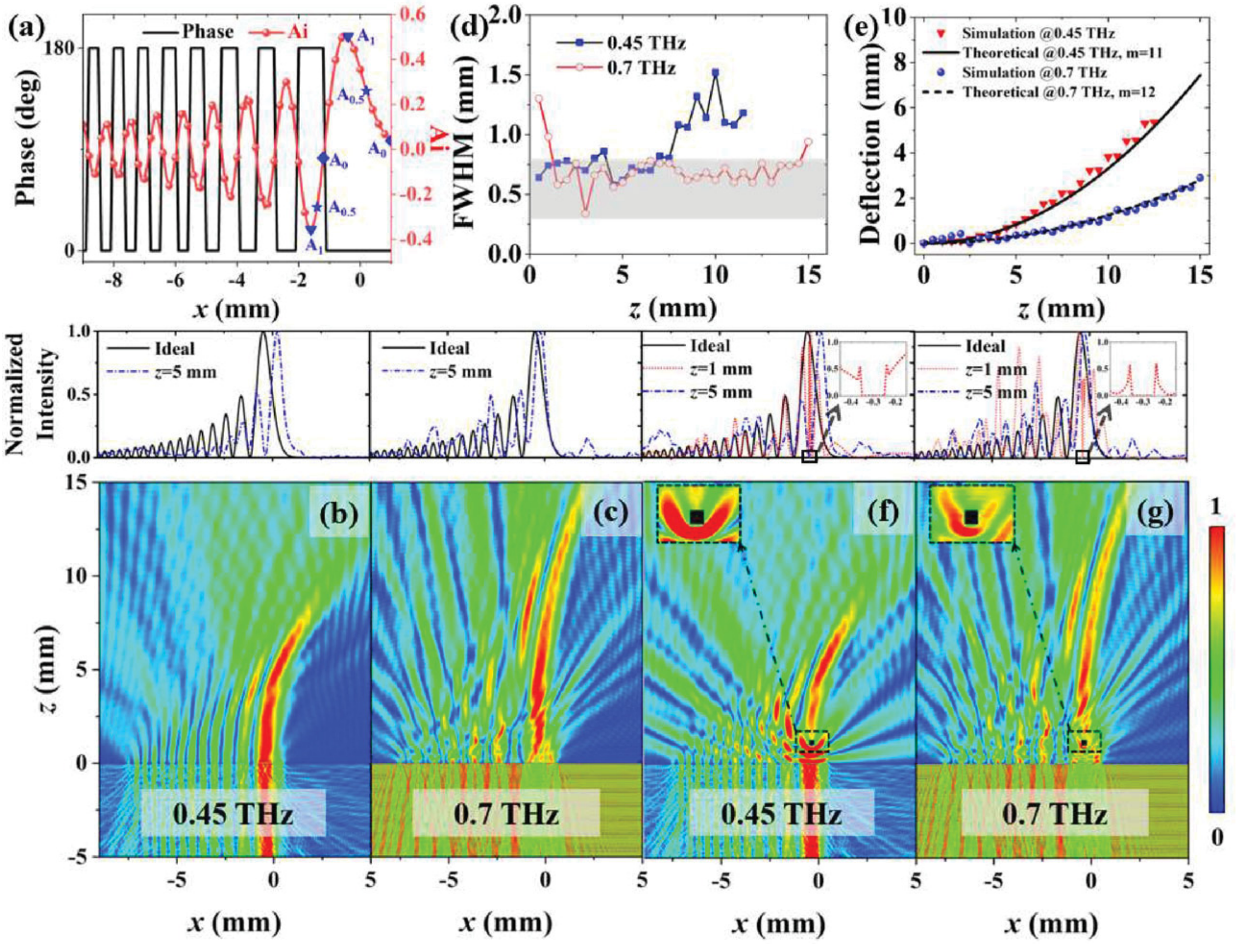

Figure 3. a) Amplitude and phase of Airy function (blue markers represent the three-level amplitude modulation). Simulated LCP electric field distributions of the Airy beam at b) 0.45 THz and c) 0.7 THz under normal RCP incidence. d) FWHM and e) deflection of the main lobe of the Airy beam with three-level amplitude modulation as functions of the propagation distance in *z*-axis. Simulated LCP electric field distributions of the Airy beam at f) 0.45 THz and g) 0.7 THz under a normal RCP incidence with a rectangular PEC obstacle of 100 μm × 100 μm in the path of the Airy main lobe.

metasurface with the theoretical maximum conversion efficiency of 0.5.[51,52] It is worth mentioning that higher conversion efficiencies can be achieved by cascading more layers.[53,54]

First, we discuss the method of generating dual-band Airy beam based on geometric metasurface. As pointed out in previous work,[30] the Airy beam with complex amplitude modulation shows better non-diffracting and more stable the full width at half maximum (FWHM); therefore, the proposed meta-atom with dual-band independent complex amplitude modulations are employed to launch the dual-band Airy beam. For generating the 1D Airy beam, the phase and amplitude profiles can be expressed as[55]

$$\phi(x,\theta) = Ai(bx)\exp(ax + ikbx\sin\theta) \tag{1}$$

where $Ai(bx) = \frac{1}{\pi}\int_0^\infty \cos(\frac{t^3}{3} + bxt)dt$ is the Airy function with x as the transverse coordinate; k denotes the wave number; θ, a, and b represent the bending direction, a positive number to truncate the Airy beam, and the transverse scale, respectively. It can be seen from Equation (1) that the amplitude distribution is only related to the position and the phase distribution is related to both position and frequency. The required phase distribution is calculated from Equation (1) as

$$\varphi = \arg[\phi(x,\theta)] = \begin{cases} kbx\sin\theta,\ Ai(bx) \geq 0 \\ \pi + kbx\sin\theta,\ Ai(bx) < 0 \end{cases} \tag{2}$$

For the 1D Airy beam generator, we consider that the bending direction is perpendicular to the metasurface (i.e., $\theta = 0°$) and $a = 0.05$, $b = 500\ \mu\text{m}^{-1}$ as a proof of concept demonstration. In this design, there are a total of 101 meta-atoms arranged in the x-axis from -9 to 1 mm. The required phase compensation is either 0 or π at each position if $\theta = \sin\theta = 0$, while the amplitude exhibits the oscillatory and exponential decaying features. **Figure 3**a plots the required phase and amplitude profiles for generating the Airy beam. The blue markers represent the three-level amplitude discretization. In this simulation, the metasurface consists of the proposed dual-band meta-atoms with the optimized geometric parameters listed in Table 1 along the x-axis, which functions at both 0.45 THz and 0.7 THz.

Throughout this work, the numerical simulations are carried out by commercial software CST and periodical and open boundary conditions are applied in the y- and x-directions, respectively. A RCP plane wave is normally illuminated on the metasurface at $z = 0$ from the substrate side (i.e., the $-z$-direction) and the LCP electric fields in the simulation domain are recorded in the XZ plane. Figure 3b,c plots the LCP electric field intensities at 0.45 THz and 0.7 THz, respectively, showing clearly the non-diffracting and self-bending features at these two frequencies. The normalized intensity distributions at $z = 5$ mm of the generated Airy beam at both frequencies are plotted on the top of Figure 3b,c, which are reasonably consistent with the ideal Airy distribution. The FWHM of the main lobe is a key parameter to evaluate the non-diffracting property of the Airy beam. Figure 3d depicts the FWHM of the Airy beam at both 0.45 and 0.7 THz. In the shadowed area, the FWHM for the propagating Airy beam remains relatively stable from the beginning to a propagation distance of 11.3 λ_1 (35 λ_2) at 0.45 THz (0.7 THz). After that, the FWHM expands quickly and the non-diffracting feature gradually vanishes. In addition, the self-bending feature of the Airy beam is another unique property. The deflection offset of the main lobe can be well described by the following equation[29]

$$\frac{\lambda_0^2}{m\pi^2 x_0^3}(z\cos\theta + x_d\sin\theta)^2 + z\sin\theta - x_d\cos\theta \cong 0 \tag{3}$$

When $\theta = 0$, Equation (3) can be approximated as

$$x_d \cong \frac{\lambda_0^2 z^2}{m\pi^2 x_0^3},\ x_0 = 0.5\ \text{mm} \tag{4}$$

The deflections of the Airy beam's main lobes at two operating frequencies are shown in Figure 3e. The main lobes of the Airy beam follow smooth trajectories in the non-diffraction zone, which agree very well with the theoretical calculations described by Equation (4).

In addition, the distinctive self-healing property of the Airy beam is investigated by placing a rectangular PEC obstacle with a size of 100 µm × 100 µm in front of the main lobe centered at (−300 µm, 1000 µm). The LCP electric field distributions with the PEC obstacle are illustrated in Figure 3f,g for 0.45 THz and 0.7 THz, respectively. The insets of Figure 3f,g show that the beam profiles could be locally modified by the introduced obstacle due to diffraction. Nevertheless, the disturbed beam profiles could be automatically corrected after passing by the obstacle. The normalized field intensity distributions at both $z = 1$ mm and $z = 5$ mm of the generated Airy beam with the obstacle at both frequencies are plotted on the top panels of Figure 3f,g. It can be observed that the field intensities at $z = 1$ mm becomes zero, crossing the PEC obstacle and gradually recovers to that of the Airy function at $z = 5$ mm.

Focusing lenses are essential elements in optical systems with extensive applications including imaging systems, displays, and detectors. Metalens has attracted much more consideration due to its flatness, compactness, and easy installation. Equation (1) reveals that the bending direction of the Airy beam can be controlled by θ, thus, we can generate an AFA beam by combining two counter-propagating Airy beams symmetrically to the origin along x-axis. When accelerating to the symmetry axis (z-axis), these two Airy beams get converged and the interference of the two main lobes results in a localized energy enhancement at different intersection points to form a focusing effect. The phase profile of an AFA beam is implemented as $\phi_{\mathrm{AFA}}(x) = \varphi(x) + \varphi(-x)$, where $\varphi(x)$ is the phase distribution described in Equation (1). For the purpose of demonstration, we set the focal point at $z = 15$ mm with a total of 251 meta-atoms, where θ is adjusted to be 18.8° (7°) for 0.45 THz (0.7 THz). The phase and amplitude profiles for 0.45 THz and 0.7 THz are provided in **Figure 4**a,b, respectively. The focusing scheme is verified by both theoretical calculations with MATLAB and full-wave simulations via CST, in which eight-level phase and three-level amplitude modulations are employed. In the theoretical calculation, the LCP electric field distribution is recorded in the XZ plane by modeling each meta-atom as a dipole-like source at $z = 0$ with proper phase and amplitude compensations obtained by Equation (2). The theoretically calculated electric field intensity at 0.45 THz (0.7 THz) is illustrated in Figure 4c (Figure 4d), which clearly shows that a maximum occurs at $z = 15$ mm from the normalized intensity along the z-axis on the right (left) side of Figure 4c (Figure 4d). In addition, the retrieved FWHMs of the normalized intensity on the focal planes are approximately 0.7 mm and 0.43 mm for 0.45 THz and 0.7 THz, respectively. The corresponding simulation results for 0.45 THz and 0.7 THz are plotted in Figure 4e,f, respectively. These two sets of results agree very well with each other, validating the design concept. In the full-wave simulation, the FWHMs are a little wider than the theoretical calculation and the focal position is also shifted a little as shown in Figure 4e, which might be caused by the non-perfect phase/amplitude modulations and the finite number of meta-atoms.

Moreover, the bending direction of the Airy beam could be adjusted to tune the focal length of an AFA beam, which is crucial in a focusing device. **Figure 5** demonstrates another two dual-band AFA beam generators with different focal lengths by adjusting the bending direction (θ). Figure 5a,b plots the calculated electric field distributions of the dual-band AFA beam with a focal length of 12.5 mm through MATLAB and CST, respectively. In this scenario, the bending angles θ are adjusted as 16.2° and 4.7° for 0.45 THz and 0.7 THz, respectively. It can be observed from Figure 5a,b that these two sets of results agree very well with each other and satisfy the design goal. Similar conclusions can be drawn for the scenario with a focal length of 17.5 mm as shown in Figure 5c,d, where the bending angles θ are set as 20.8° and 8.8° for 0.45 THz and 0.7 THz, respectively. In each plot of Figure 5, the field intensities along the focal plane (dashed line) and the optical axis ($z = 0$) are plotted on the top and left/right side. It can be seen from Figures 4 and 5 that the DOF is proportional to the focal length, which originates from the longer interference region for the two Airy beams with larger deflection angles. In addition, the FWHM is also proportional to the bending direction (θ).

Furthermore, we plot the focus distance (FD) versus the bending direction with an interval of 0.5° from 0° to 20° in **Figure 6** together with the polynomial fitting equations for both 0.45 THz and 0.7 THz, which are given in Equations (5) and (6), respectively. In addition, it is noticed that a smaller wavelength requires a smaller bending direction for a fixed focus distance.

$$\mathrm{FD}_{0.45THz} = 5.13 + 0.118\theta + 0.00212\theta^2 \tag{5}$$

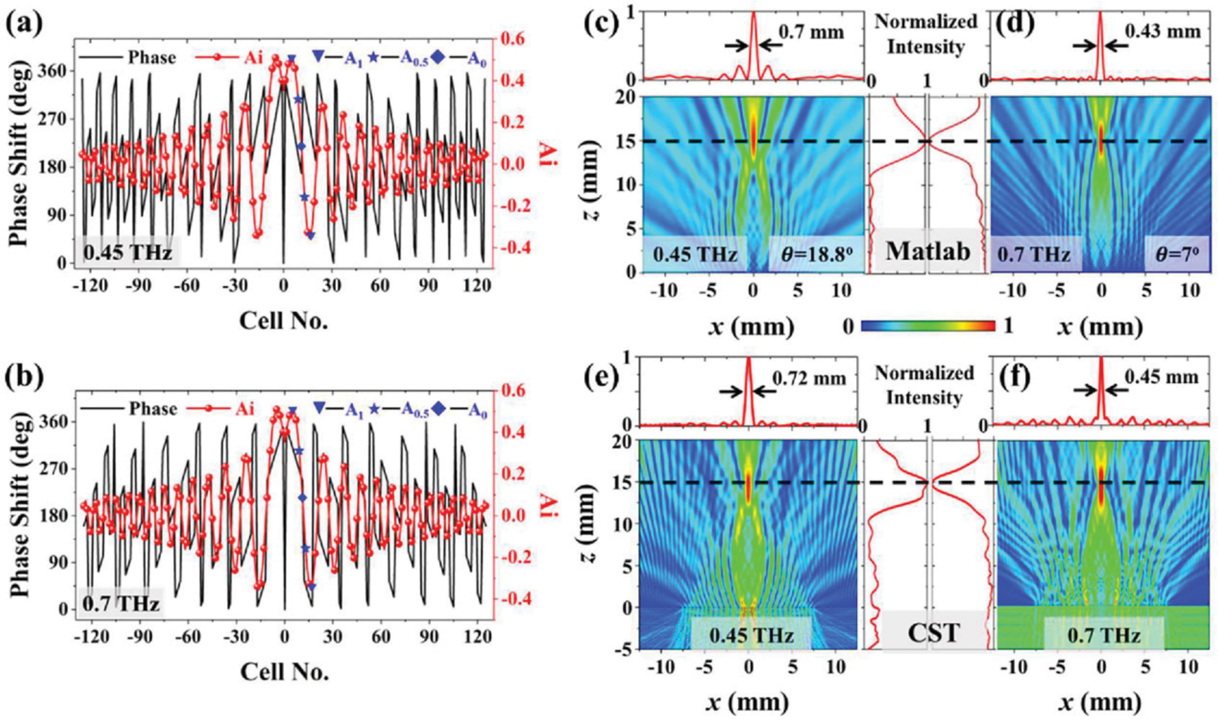

Figure 4. The phase and amplitude profiles for the AFA beam at a) 0.45 THz and b) 0.7 THz; the theoretical calculated LCP electric field distribution at c) 0.45 THz and d) 0.7 THz under a RCP incidence; the numerical simulated LCP electric field distribution at e) 0.45 THz and f) 0.7 THz under a RCP incidence.

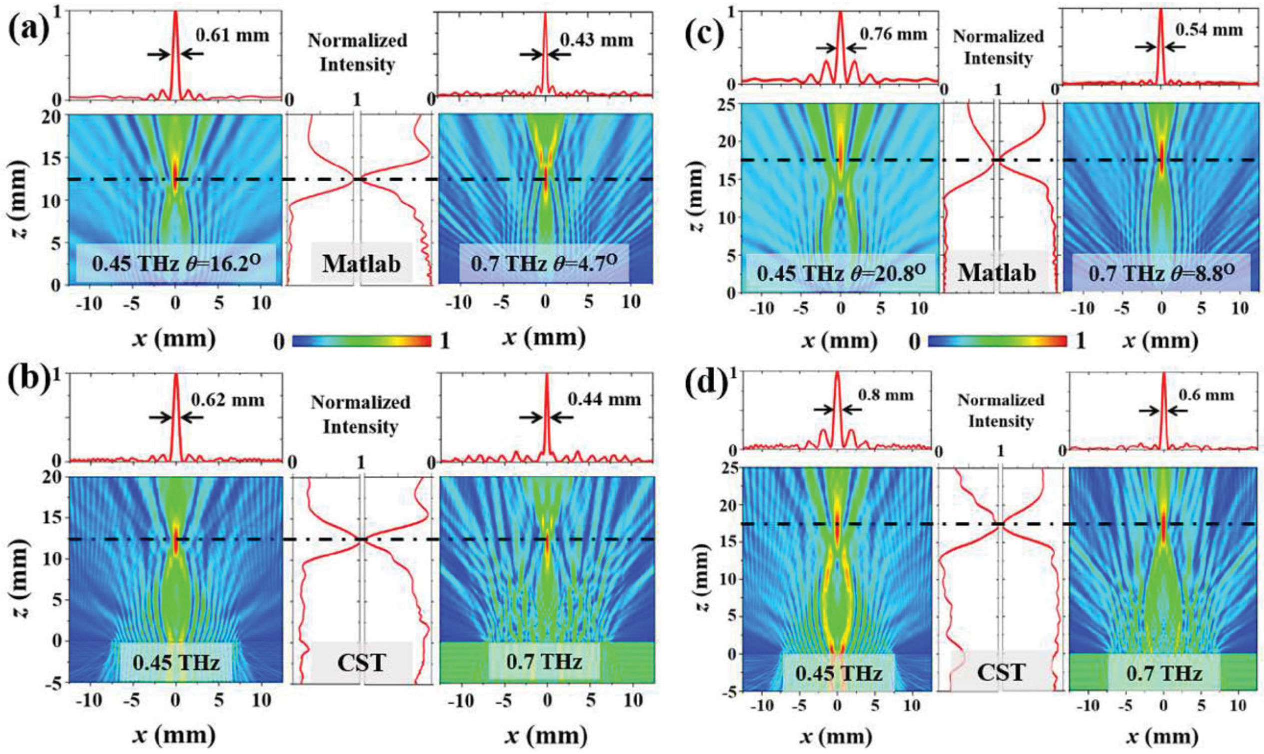

Figure 5. The LCP electric field distribution of the autofocusing Airy beam under a RCP incidence through a) theoretical calculations and b) full-wave simulations at 0.45 THz and 0.7 THz with $f = 12.5$ mm. c) Theoretical calculations and d) full-wave simulations at 0.45 THz and 0.7 THz with $f = 17.5$ mm.

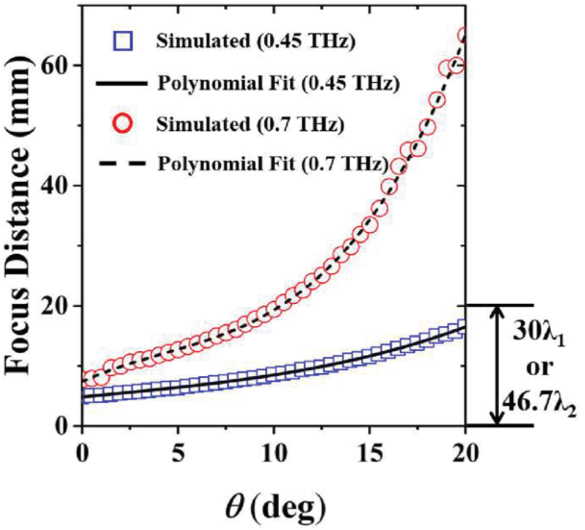

Figure 6. The simulated and fitted focus distance versus different bending direction at 0.45 THz and 0.7 THz.

$$\mathrm{FD}_{0.7THz} = 7.41 + 1.44\theta - 0.123\theta^2 + 0.00977\theta^3 \tag{6}$$

In order to make comparison with the proposed AFA beam, we also study a conventional dual-band spherical metalens. In the conventional metalens, a hyperboloidal phase profile is required to compensate the phase differences according to the equal optical path principle, which can be expressed as

$$\varphi(r, \lambda_i) = -\frac{2\pi}{\lambda_i}\left(\sqrt{r^2 + f^2} - f\right), \quad \text{for } i = 1, 2 \tag{7}$$

where $\varphi(r, \lambda_i)$ represents the required phase compensation between an arbitrary point $r^2 = x^2 + y^2$ and the original point O at the incident wavelength of λ_i, and f is the focal length. A dual-band conventional spherical metalens is designed with the proposed meta-atoms, which is demonstrated in Figure S1, Supporting Information. Figure S1a,b, Supporting Information plot the required and digitized phase profiles for a metalens with a focal length of $f = 15$ mm at 0.45 THz and 0.7 THz, respectively, with a total number of 251 meta-atoms. The calculated and simulated LCP electric field distributions are plotted in Figure S1c–f, Supporting Information, which clearly demonstrate that the incident RCP wave is well focused at the preset focal point at both 0.45 THz and 0.7 THz. As can be seen from Figure 4 and Figure S1, Supporting Information, the AFA beam has a little larger DOF compared to the conventional metalens, which could be intriguing for various practical applications such as medical imaging and nondestructive detections.

Next, we will demonstrate the distinctive self-healing ability of the AFA beam to circumvent certain PEC scatterers or obstacles, which could be of great importance in various applications with obstacles in the propagation path. To investigate how the focusing effect of an AFA beam would be affected by the presence of obstacles with nontrivial sizes, several cases with different obstacles are studied for both dual-band conventional metalens and AFA beam with a focal length of 15 mm at 0.45 THz and 0.7 THz, four of which are demonstrated in **Figure 7**. The dual-band conventional metalens and AFA beam generator are both designed by the proposed meta-atoms and shown in previous paragraphs. The sizes and center positions of the obstacles for these four cases are listed in **Table 2**. Some other cases are depicted in Figure S2, Supporting Information.

Figure 7a,b plots the electric field intensities obtained by the conventional spherical metalens and AFA beam at both 0.45 THz and 0.7 THz for Case 1, respectively. In Case 1, the obstacle with a size of 1.5 mm × 1.5 mm is centered at (0, 3.25 mm), which is symmetrical to the z-axis, thus, the contributions from the meta-atoms on $-x$-axis and x-axis are still identical for both focusing devices (although the diffractions occur), resulting in good focusing effects with a little change on FWHM and DOF. The results for Case 2 are illustrated in Figure 7c,d for the conventional metalens and AFA beam, respectively, where the obstacle with a larger size of 6 mm × 0.5 mm is centered at (−8 mm, 0.75 mm). As can be seen from Figure 7c, the obstacle is close to the metasurface at $z = 0$ and on the left side, which is not symmetric to the z-axis, thus, most of the contributions of the meta-atoms beneath the obstacle are blocked or suppressed for the conventional metalens, resulting in tilted focusing areas (leaning toward the obstacle) and enlarged focusing spots at both working frequencies. The tilting effect could be intuitively explained by the fact that the interference occurs mainly among the unblocked meta-atoms and the contributions from the blocked meta-atoms are trivial. The tilting could greatly deteriorate the imaging quality in an optical system, while for the AFA beam, due to the self-healing ability, good focusing effects can be observed in Figure 7d at both frequencies. Figure 7e,f demonstrates the results for Case 3, where an obstacle with a moderate size of 3 mm × 0.5 mm is centered at (−4.5 mm, 3.25 mm). For the conventional metalens, Figure 7e clearly shows that the contributions from the meta-atoms beneath the obstacle are partially reflected and diffracted, resulting in tilted and sliced focusing areas after combining the contributions from the rest of meta-atoms at both frequencies. The disturbance becomes worse at 0.7 THz. However, although the electromagnetic wave is partially reflected and diffracted, the dual-band AFA beam can still reconverge to the designed focal area with good focusing effects at both frequencies due to the distinctive self-healing property, as shown in Figure 7f. Furthermore, similar conclusions to Case 3 can be drawn for Case 4, in which another small obstacle is added to Case 3. Due to the additional small obstacle, as can be seen from Figure 7g, the focusing effects at both frequencies are further disturbed due to the strong interference for the conventional metalens, especially at 0.7 THz. On the contrary, good focusing effects at both frequencies can still be observed for the AFA beam, and the results are very close to those of Case 3. Furthermore, several more scenarios with different obstacles for the proposed AFA beam and the conventional metalens are compared in Figure S2, Supporting Information. These studies further reveal the distinctive self-healing feature of the Airy beam generator.

In summary, a general scheme is proposed for generating the dual-band Airy beam and AFA beam based on the geometric metasurface with independent complex amplitude modulations at two THz frequencies. The metasurface is composed of a novel dual-band single-layer meta-atom, which consists of a MDCS resonator and an elliptic nanorod resonator located in the middle of a circular hole. The independent complex amplitude modulations at two THz frequencies can be obtained by varying

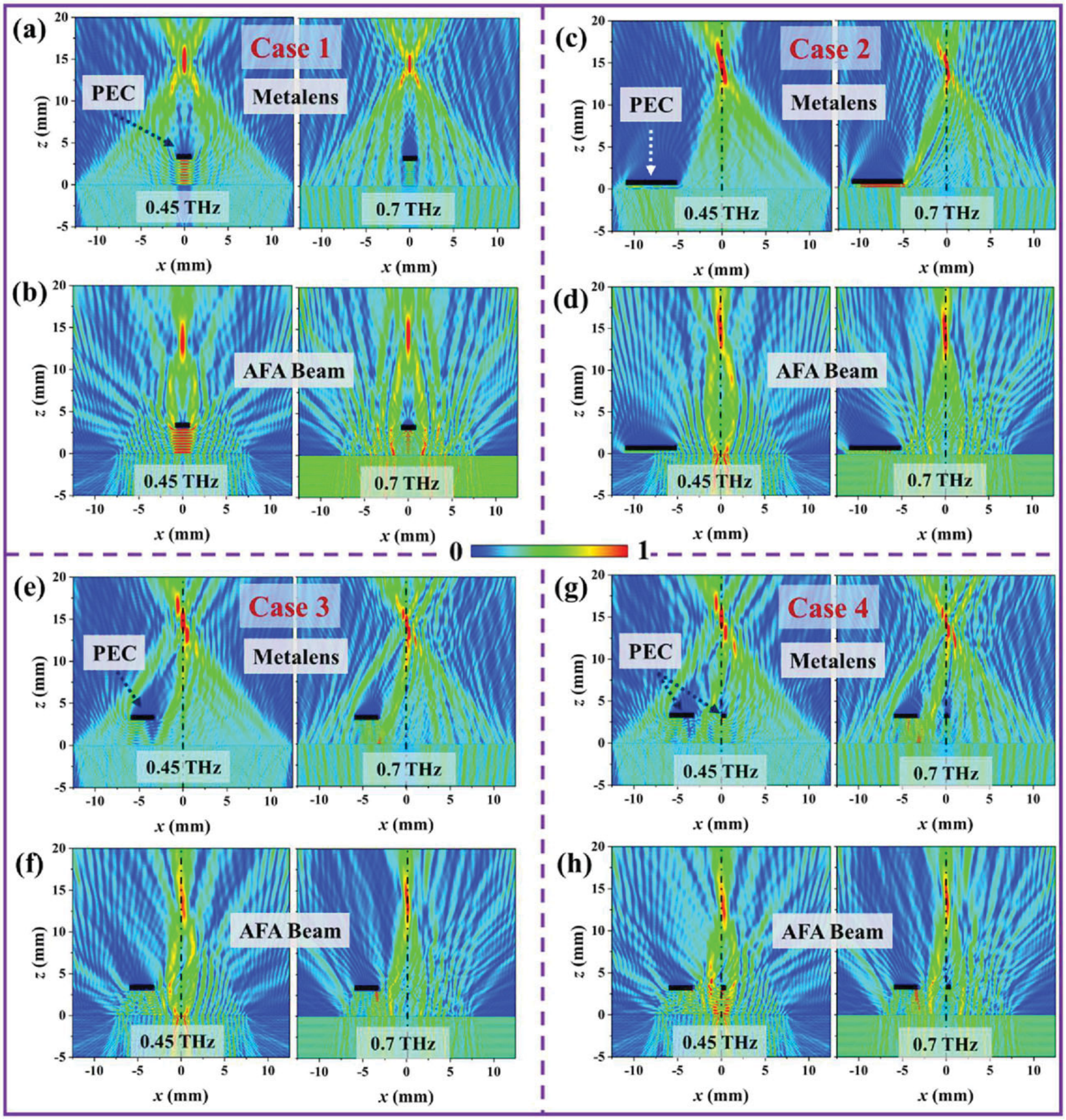

Figure 7. The LCP electric field intensity distributions of a dual-band conventional metalens and AFA beam with different obstacles under a RCP incidence: a,b) obstacle size of 1.5 × 0.5, center (0, 3.25); c,d) size of 6 × 0.5, center (−8, 0.25); e,f) size of 3 × 0.5, center (−4.5, 3.25); g,h) obstacle 1 size of 3 × 0.5, center (−4.5, 3.25), obstacle 2 size of 0.5 × 0.5, center (0.25, 3.25). (unit: mm).

Table 2. The sizes and positions of the obstacles for four investigated cases.

	Obstacle size [mm]	Obstacle center position [mm]
Case 1	1.5 × 1.5	(0, 3.25)
Case 2	6 × 0.5	(−8, 0.75)
Case 3	3 × 0.5	(−4.5, 3.25)
Case 4	3 × 0.5 and 0.5 × 0.5	(−4.5, 3.25) and (0.25, 3.25)

the dimensions and orientations of the two types of resonators. The circular hole could add another degree of freedom to finely tune the coupling between the two resonators and adjust the amplitude modulations. The non-diffracting, self-bending, and self-healing features of the dual-band Airy beam are characterized through full-wave simulation at both 0.45 THz and 0.7 THz, which are in good agreement with the design goals. Moreover, a new kind of dual-band metalens (i.e., the AFA beam) can be achieved by combining two counter-propagating Airy beams, which is validated through both theoretical calculations and full-wave simulations. The focal length of the proposed dual-band metalens can be flexibly manipulated by assigning proper bending angles at each frequency. Furthermore, compared to the conventional metalens through a number of scenarios with different PEC obstacles, the proposed metalens shows a much better capability of circumventing obstacles in the path due to its self-healing feature. In contrast to previous approaches for generating Airy beams and AFA beams, the proposed scheme features many attractive features such as the compactness of the system and the multiband characteristic due to the novel meta-atom design. The proposed dual-band Airy beams and AFA beams with distinctive properties of self-healing and self-bending could open new avenues for many emerging applications such as multiband wave manipulation, imaging and remote power transmission with obstacles, and THz communications.

Supporting Information

Supporting Information is available from the Wiley Online Library or from the author.

Acknowledgements

W. T. and G. Z. contributed equally to this work. This work was supported by the Natural Science Foundation of Shanghai (Grant 16ZR1445800), Shanghai Pujiang Program (Grant 18PJ1403200), and a research grant from the U.S. National Science Foundation (1661749).

Conflict of Interest

The authors declare no conflict of interest.

Keywords

Airy beams, auto-focusing Airy beams, complex amplitude modulations, dual-band meta-atoms

Received: April 8, 2019

[1] M. V. Berry, N. L. Balazs, *Am. J. Phys.* **1979**, *47*, 264.
[2] G. A. Siviloglou, D. N. Christodoulides, *Opt. Lett.* **2007**, *32*, 979.
[3] G. A. Siviloglou, J. Broky, A. Dogariu, D. N. Christodoulides, *Phys. Rev. Lett.* **2007**, *99*, 213901.
[4] N. K. Efremidis, D. N. Christodoulides, *Opt. Lett.* **2010**, *35*, 4045.
[5] D. G. Papazoglou, N. K. Efremidis, D. N. Christodoulides, S. Tzortzakis, *Opt. Lett.* **2011**, *36*, 1842.
[6] J. Baumgartl, M. Mazilu, K. Dholakia, *Nat. Photonics* **2008**, *2*, 675.
[7] P. Panagiotopoulos, D. G. Papazoglou, A. Couairon, S. Tzortzakis, *Nat. Commun.* **2013**, *4*, 2622.
[8] G. A. Siviloglou, J. Broky, A. Dogariu, D. N. Christodoulides, *Opt. Lett.* **2008**, *33*, 207.
[9] J. Broky, G. A. Siviloglou, A. Dogariu, D. N. Christodoulides, *Opt. Express* **2008**, *16*, 12880.
[10] B.-Y. Wei, P. Chen, W. Hu, W. Ji, L.-Y. Zheng, S.-J. Ge, Y. Ming, V. Chigrinov, Y.-Q. Lu, *Sci. Rep.* **2015**, *5*, 17484.
[11] N. Yu, P. Genevet, M. A. Kats, F. Aieta, J.-P. Tetienne, F. Capasso, Z. Gaburro, *Science* **2011**, *334*, 333.
[12] N. Yu, F. Capasso, *Nat. Mater.* **2014**, *13*, 139.
[13] S. B. Glybovski, S. A. Tretyakov, P. A. Belov, Y. S. Kivshar, C. R. Simovski, *Phys. Rep.* **2016**, *634*, 1.
[14] M. I. Shalaev, J. Sun, A. Tsukernik, A. Pandey, K. Nikolskiy, N. M. Litchinitser, *Nano Lett.* **2015**, *15*, 6261.
[15] M. Pu, X. Li, X. Ma, Y. Wang, Z. Zhao, C. Wang, C. Hu, P. Gao, C. Huang, H. Ren, X. Li, F. Qin, J. Yang, M. Gu, M. Hong, X. Luo, *Sci. Adv.* **2015**, *1*, e1500396.
[16] M. Q. Mehmood, S. Mei, S. Hussain, K. Huang, S. Y. Siew, L. Zhang, T. Zhang, X. Ling, H. Liu, J. Teng, A. Danner, S. Zhang, C.-W. Qiu, *Adv. Mater.* **2016**, *28*, 2533.
[17] W. T. Chen, M. Khorasaninejad, A. Y. Zhu, J. Oh, R. C. Devlin, A. Zaidi, F. Capasso, *Light: Sci. Appl.* **2017**, *6*, e16259.
[18] X. Ni, Z. J. Wong, M. Mrejen, Y. Wang, X. Zhang, *Science* **2015**, *349*, 1310.
[19] Y. Yang, L. Jing, B. Zheng, R. Hao, W. Yin, E. Li, C. M. Soukoulis, H. Chen, *Adv. Mater.* **2016**, *28*, 6866.
[20] N. Han, L. Huang, Y. Wang, *Opt. Express* **2018**, *26*, 31625.
[21] F. Aieta, P. Genevet, M. A. Kats, N. Yu, R. Blanchard, Z. Gaburro, F. Capasso, *Nano Lett.* **2012**, *12*, 4932.
[22] A. Arbabi, Y. Horie, A. J. Ball, M. Bagheri, A. Faraon, *Nat. Commun.* **2015**, *6*, 7069.
[23] M. Khorasaninejad, W. T. Chen, R. C. Devlin, J. Oh, A. Y. Zhu, F. Capasso, *Science* **2016**, *352*, 1190.
[24] W. T. Chen, A. Y. Zhu, M. Khorasaninejad, Z. Shi, V. Sanjeev, F. Capasso, *Nano Lett.* **2017**, *17*, 3188.
[25] L. Huang, X. Chen, H. Mühlenbernd, H. Zhang, S. Chen, B. Bai, Q. Tan, G. Jin, K.-W. Cheah, C.-W. Qiu, J. Li, T. Zentgraf, S. Zhang, *Nat. Commun.* **2013**, *4*, 2808.
[26] X. Ni, A. V. Kildishev, V. M. Shalaev, *Nat. Commun.* **2013**, *4*, 2807.
[27] G. Zheng, H. Mühlenbernd, M. Kenney, G. Li, T. Zentgraf, S. Zhang, *Nat. Nanotechnol.* **2015**, *10*, 308.
[28] L. Li, T. Jun Cui, W. Ji, S. Liu, J. Ding, X. Wan, Y. Bo Li, M. Jiang, C.-W. Qiu, S. Zhang, *Nat. Commun.* **2017**, *8*, 197.
[29] Q. Fan, D. Wang, P. Huo, Z. Zhang, Y. Liang, T. Xu, *Opt. Express* **2017**, *25*, 9285.
[30] Z. Li, H. Cheng, Z. Liu, S. Chen, J. Tian, *Adv. Opt. Mater.* **2016**, *4*, 1230.
[31] J. Ding, S. An, B. Zheng, H. Zhang, *Adv. Opt. Mater.* **2017**, *5*, 1700079.
[32] Z. Li, K. Yao, F. Xia, S. Shen, J. Tian, Y. Liu, *Sci. Rep.* **2015**, *5*, 12423.
[33] E.-Y. Song, G.-Y. Lee, H. Park, K. Lee, J. Kim, J. Hong, H. Kim, B. Lee, *Adv. Opt. Mater.* **2017**, *5*, 1601028.
[34] W. T. Chen, A. Y. Zhu, V. Sanjeev, M. Khorasaninejad, Z. Shi, E. Lee, F. Capasso, *Nat. Nanotechnol.* **2018**, *13*, 220.
[35] S. Wang, P. C. Wu, V.-C. Su, Y.-C. Lai, M.-K. Chen, H. Y. Kuo, B. H. Chen, Y. H. Chen, T.-T. Huang, J.-H. Wang, R.-M. Lin, C.-H. Kuan, T. Li, Z. Wang, S. Zhu, D. P. Tsai, *Nat. Nanotechnol.* **2018**, *13*, 227.
[36] S. Shrestha, A. C. Overvig, M. Lu, A. Stein, N. Yu, *Light: Sci. Appl.* **2018**, *7*, 85.
[37] X. Zhang, Z. Tian, W. Yue, J. Gu, S. Zhang, J. Han, W. Zhang, *Adv. Mater.* **2013**, *25*, 4567.
[38] Q. Wang, X. Zhang, Y. Xu, J. Gu, Y. Li, Z. Tian, R. Singh, S. Zhang, J. Han, W. Zhang, *Sci. Rep.* **2016**, *6*, 32867.
[39] L. Huang, X. Chen, H. Mühlenbernd, G. Li, B. Bai, Q. Tan, G. Jin, T. Zentgraf, S. Zhang, *Nano Lett.* **2012**, *12*, 5750.
[40] X. Su, C. Ouyang, N. Xu, W. Cao, X. Wei, G. Song, J. Gu, Z. Tian, J. F. O'Hara, J. Han, W. Zhang, *Opt. Express* **2015**, *23*, 27152.
[41] X. Zhang, J. Jin, Y. Wang, M. Pu, X. Li, Z. Zhao, P. Gao, C. Wang, X. Luo, *Sci. Rep.* **2016**, *6*, 19856.

[42] E. Arbabi, A. Arbabi, S. M. Kamali, Y. Horie, A. Faraon, *Sci. Rep.* **2016**, *6*, 32803.
[43] E. Maguid, I. Yulevich, D. Veksler, V. Kleiner, M. L. Brongersma, E. Hasman, *Science* **2016**, *352*, 1202.
[44] M. Kang, T. Feng, H.-T. Wang, J. Li, *Opt. Express* **2012**, *20*, 15882.
[45] S. Pancharatnam, *Proc. Indian Acad. Sci. - Sect. A* **1956**, *44*, 247.
[46] M. V. Berry, *Proc. R. Soc. A* **1984**, *392*, 45.
[47] L. Huang, H. Mühlenbernd, X. Li, X. Song, B. Bai, Y. Wang, T. Zentgraf, *Adv. Mater.* **2015**, *27*, 6444.
[48] X. Ding, F. Monticone, K. Zhang, L. Zhang, D. Gao, S. N. Burokur, A. de Lustrac, Q. Wu, C.-W. Qiu, A. Alù, *Adv. Mater.* **2015**, *27*, 1195.
[49] X. Luo, *Sci. China: Phys., Mech. Astron.* **2015**, *58*, 594201.
[50] J. Ding, N. Xu, H. Ren, Y. Lin, W. Zhang, H. Zhang, *Sci. Rep.* **2016**, *6*, 34020.
[51] F. Monticone, N. M. Estakhri, A. Alù, *Phys. Rev. Lett.* **2013**, *110*, 203903.
[52] A. Arbabi, A. Faraon, *Sci. Rep.* **2017**, *7*, 43722.
[53] S. Liu, Q. Cheng, Q. Xu, T. Q. Wang, L. L. Du, K. Luan, Y. H. Xu, D. Bao, X. J. Fu, J. G. Han, W. L. Zhang, T. J. Cui, *Adv. Opt. Mater.* **2016**, *4*, 384.
[54] Y. Guo, X. Ma, M. Pu, X. Li, Z. Zhao, X. Luo, *Adv. Opt. Mater.* **2018**, *6*, 1800592.
[55] H. Gao, Z. Gu, B. Liang, X. Zou, J. Yang, J. Yang, J. Cheng, *Appl. Phys. Lett.* **2016**, *108*, 073501.